Detailed Reaction Mechanisms for the Oxidative Coupling of Methane over La$_2$O$_3$/CeO$_2$ Nanofiber Fabric Catalysts

Canan Karakaya,*[a] Huayang Zhu,[a] Bahman Zohour,[b] Selim Senkan,[b] and Robert J. Kee[a]

We develop and validate detailed reaction mechanisms to represent the oxidative coupling of methane (OCM) over a La$_2$O$_3$/CeO$_2$ nanofabric catalyst. The reaction mechanism includes 39 reversible gas-phase reactions and 52 irreversible surface reactions between 22 gas-phase species and 11 surface species. We use a model-based interpretation of spatially resolved concentration and temperature profiles measured by using a laboratory-scale packed-bed reactor. The reaction mechanisms are validated for inlet feed compositions in the range of $7 \leq$ CH$_4$/O$_2 \leq 11$. The results are supported by a reaction pathway analysis that provides insight into the relative contributions of the gas-phase and surface reactions to form the desired C$_{2+}$ and the undesired CO$_x$ products. The results provide new quantitative insights into the complex nature of the OCM chemistry, which can assist practical process and reactor development.

1. Introduction

The catalytic oxidative coupling of methane (OCM) is a process in which methane and oxygen react over a catalyst to produce ethylene, ethane, and other C$_3$ products. The OCM process is a potentially viable route to convert natural gas to more valuable higher hydrocarbons and petrochemical feedstocks. The objective of this study is to develop detailed reaction mechanisms that represent the process quantitatively over La$_2$O$_3$/CeO$_2$ catalysts. The reaction mechanisms include multiple elementary homogeneous gas-phase reactions coupled with multiple heterogeneous surface reactions. Such validated reaction mechanisms can be used to understand the complexities of the OCM reaction process and thus to assist the design and development of OCM reactors and practical technology.

Discovered by Keller and Bhasin in 1982,[1] the OCM process can be represented globally as [Eq. (1)]:

$$2\,CH_4 + O_2 \rightarrow C_2H_4 + 2\,H_2O \qquad \Delta H_\circ^{298} \approx -281\,kJ\,mol^{-1} \qquad (1)$$

The major desired product C$_2$H$_4$ has numerous industrial applications. For example, C$_2$H$_4$ is the monomer of polyethylene and an important component of some logistics fuels. The oligomerization of ethylene can contribute to the production of gasoline (C$_5$–C$_{10}$) or diesel fuel (C$_{10}$–C$_{20}$).[2,3] Current OCM processes have C$_2$H$_4$ yields of approximately 10–15%, which is significantly lower than the 25% yield that has been reported to be commercially viable.[4,5] In addition to the desired C$_2$H$_4$ product, the OCM reaction also produces considerable amounts of C$_2$H$_6$. The gas-phase C$_3$ yields (C$_3$H$_6$ and C$_3$H$_8$) are generally below 1%. The dehydrogenation of CH$_4$, C$_2$H$_4$, and C$_2$H$_6$ also produces H$_2$ yields in the range of 1–5%. All these side products have industrial value but require separation. To date, despite the potential value, there has been only limited commercial development of the OCM process.

The OCM reaction products and their distributions depend on the operating temperature and the catalyst. The role of the catalyst is primarily to initiate methane activation by the abstraction of one hydrogen atom from methane with surface oxygen species and the suppression of deep oxidation to CO$_x$ and H$_2$O. A number of catalysts are active for OCM, which include Mn/Na$_2$WO$_4$/SiO$_2$, La$_2$O$_3$, and Li/MgO. These catalysts are active at elevated temperatures, typically 700–850 °C. The criteria for the selection of a particular catalyst include stability and durability as well as C$_{2+}$ (i.e., C$_2$ and C$_3$) selectivities and yields. The catalysts are implemented typically in packed-bed configurations.

Major design and operational challenges are associated with controlling the formation of undesired deep-oxidation products (i.e., CO, CO$_2$, and H$_2$O). The CO$_x$ species not only decrease the desired C$_2$ carbon yields but also contribute to downstream separation costs.[6,7] Unfortunately, under elevated temperature and oxidizing environments, the full oxidation of CH$_4$ and the desired C$_2$ species is thermodynamically more favorable than the pathway to the desired ethylene. A practically successful OCM process must avoid the full oxidation of the parent CH$_4$ and the produced C$_2$H$_4$.

The global OCM reaction [Eq. (1)] shows a stoichiometric ratio of CH$_4$/O$_2 = 2$. However, to avoid deep oxidation, practical reactors must operate in the range of $5 \leq$ CH$_4$/O$_2 \leq 10$. The CH$_4$ conversion is controlled by the O$_2$ in the feed mixture, and

[a] Prof. C. Karakaya, H. Zhu, R. J. Kee
Mechanical Engineering
Colorado School of Mines
Golden, CO 80401 (USA)
E-mail: ckarakay@mines.edu

[b] Dr. B. Zohour, S. Senkan
Department of Chemical and Biomolecular Engineering
University of California
Los Angeles, CA 90095 (USA)

Supporting Information and the ORCID identification number(s) for the author(s) of this article can be found under https://doi.org/10.1002/cctc.201701172.

higher oxygen levels contribute to a greater conversion. However, high O_2 levels tend to increase the reactor temperature and the undesired full oxidation.

On one hand, high temperature promotes the desired non-oxidative CH_3–H activation, which increases the $CH_3^{\bullet}$ formation and rapid $CH_3^{\bullet}$ recombination to form desired C_2. On the other hand, temperatures that are too high promote competing deep oxidation by both gas-phase and surface reactions. Optimization of the operating temperature to promote methane dehydrogenation but prevent deep oxidation, depends greatly on the particular catalyst, the feed-mixture composition, and flow rates.

Practical packed-bed reactors do not operate isothermally (i.e., the temperature varies throughout the bed), and an elevated temperature is needed to initiate methane activation. However, exothermic oxidation contributes to undesired temperature increases that promote deep oxidation. Additionally, excessive temperatures and local temperature excursions can damage the catalyst and the reactor. Reactor design and control can benefit from an improved understanding of the fundamental chemistry as represented by detailed reaction mechanisms. The results of the present models suggest design strategies that use staged oxygen addition or oxygen permselective membranes to assist thermal control and thus improve OCM processes.

1.1. La$_2$O$_3$-based catalysts

La_2O_3 is an OCM catalyst with a high C_2 selectivity. Unfortunately, it is unstable above $600\,°C$ and thus is not technologically practical. La_2O_3 reacts with CO_2 to form a dioxymonocarbonate structure at temperatures above $650\,°C$ [Eq. (2)]:[8,9]

$$La_2O_3 + CO_2 \rightarrow La_2O_2CO_3 \tag{2}$$

The $La_2O_2CO_3$ phase is also an active OCM catalyst but it is unstable at temperatures $>850\,°C$.[9] Depending on how an OCM reactor is designed and controlled, local temperatures can exceed $850\,°C$.

Despite the drawbacks, La_2O_3 is a relatively simple oxide (compared, for example, to $Mn/Na_2WO_4/SiO_2$) and is used widely on a laboratory scale to study OCM chemistry.[10–16] As a result of recent advances in variants of La_2O_3, there is good reason to revisit La_2O_3 as a potentially viable OCM catalyst.

Nanofabric catalyst synthesis is known to increase catalyst stability and reduce operating temperatures below $600\,°C$.[14,16–18] Hou et al.[16] studied $La_2O_3CO_3$ catalysts with different nanoscale plate and rod morphologies, particle sizes, and calcination temperatures. The measured catalyst performance in a packed-bed reactor at atmospheric pressure and $420\,°C$ showed 30% CH_4 conversion and 50% C_{2+} selectivity. The $La_2O_3CO_3$ catalyst was stable for over 50 h.

The C_2 selectivity and OCM yield can be increased by doping La_2O_3 catalysts with alkaline earth metals (Sr, Mg, Ca) that produce strong basic sites.[10,13,19] Early studies indicated that Sr doping showed the most promising OCM activity.[11,12,20] Choudhary et al.[13] reported a 17% C_2 yield over $Sr-La_2O_3$ at

$800\,°C$ in a continuous-flow packed-bed reactor. Song et al.[18] developed a stable $Sr-La_2O_3$ nanofiber catalyst, which produced approximately 16% C_2 yield at $500\,°C$ and was stable up to $800\,°C$.

Noon et al.[17] showed that La_2O_3/CeO_2 nanofabric catalysts delivered superior OCM performance compared to the same catalyst compositions in powder form. Based on packed-bed reactor measurements, Noon et al. reported a maximum of 16% C_{2+} yield at $620\,°C$.[17] Additionally, the La_2O_3/CeO_2 catalyst was found to be coke tolerant. Based in large measure on the results of Noon et al.,[17] in the present study we focus on the development of detailed reaction mechanisms to represent OCM chemistry for La_2O_3/CeO_2 nanofiber fabric catalysts.

2. Previous studies on OCM reaction kinetics

Although OCM is generally understood to be a catalytic process, it does depend on synergistic gas-phase chemistry. Especially above $600\,°C$, homogeneous gas-phase chemistry produces C_2H_4 and C_2H_6 without a catalyst. The relative importance of gas-phase chemistry depends on residence time and pressure, as well as the CH_4/O_2 ratio in the feed stream.[21–23] Experimental studies show that C_2 formation rates depend strongly on $CH_3^{\bullet}$ concentrations.[10,12,20,24–27] The increase of the reaction temperature and pressure increases the formation rate of methyl radicals almost independent of the particular catalyst. However, in low-pressure regimes, the methyl radical formation rate depends weakly on temperature, but varies significantly depending upon the particular catalyst. As the catalyst increases the methyl radical formation rate, it also increases the C_2 formation rate.

Multistep global reactions have been developed, modified, and applied to model OCM chemistry. The most widely used reaction mechanism is a 10-step mechanism that was proposed in 1997 by Stansch et al.[19] The Stansch catalytic reaction mechanism involves only gas-phase species (i.e., it does not involve surface adsorbates explicitly; Table 1). The relatively complicated empirical rate expressions implicitly incorporate parameters and functional dependencies that represent the catalyst. Although the Stansch model was developed for a La_2O_2/CaO catalyst, it has been modified and adapted to represent other OCM catalysts (e.g., $Mn/Na_2WO_4/SiO_2$) by tuning the

Table 1. Global reactions for OCM processes reported by Stansch et al.[19]

	Reaction	$\approx \Delta H_{298}^{\circ}$ [kJ]
1.	$CH_4 + 2O_2 \rightarrow CO_2 + 2H_2O$	−802
2.	$2CH_4 + \frac{1}{2}O_2 \rightarrow C_2H_6 + H_2O$	−177
3.	$CH_4 + O_2 \rightarrow CO + H_2O + H_2$	−277
4.	$CO + \frac{1}{2}O_2 \rightarrow CO_2$	−283
5.	$C_2H_6 + \frac{1}{2}O_2 \rightarrow C_2H_4 + H_2O$	−105
6.	$C_2H_4 + 2O_2 \rightarrow 2CO + 2H_2O$	−757
7.	$C_2H_6 \rightarrow C_2H_4 + H_2$	+137
8.	$C_2H_4 + 2H_2O \rightarrow 2CO + 4H_2$	+210
9.	$CO + H_2O \rightarrow CO_2 + H_2$	−41
10.	$CO_2 + H_2 \rightarrow CO + H_2O$	+41

individual rate expressions to fit measured packed-bed reactor performance.

Although lumped kinetic models (e.g., Stansch) are used to assist reactor development, they provide only a limited insight into the fundamental chemistry and have limited predictive capability. Compared to lumped kinetic models, detailed reaction mechanisms can provide a much richer description of the chemistry and can capture a larger range of processes. Although the development of the elementary reaction pathways and rate expressions can be challenging, a validated elementary mechanism has great practical benefits.

Thybaut et al. have developed reaction mechanisms for several OCM catalysts, which include Sr/La_2O_3, $LaSr/CaO$, $NaMnW/SiO_2$, Li/MgO, and $Sn-Li/MgO$.[28–32] However, to date, there are no published reaction mechanisms for La_2O_3/CeO_2 catalysts. In this study, we develop and validate a reaction mechanism for La_2O_3/CeO_2 nanofabric catalysts.

2.1. OCM reaction pathways

Both gas-phase and surface reactions play significant roles for CH_4 activation as well as C_{2+} and CO_x formation. Despite differences in the active catalytic sites for particular catalysts, it is generally known that the methane activation proceeds via the $CH_3^{\bullet}$ radical. The initiating $CH_3^{\bullet}$ formation reactions control the overall reaction rate.

Gas-phase chemistry contributes to $CH_3^{\bullet}$ formation by both oxidative and nonoxidative reactions, which are generally know from combustion research.[4,33–36] In the gas phase, methane can be attacked by either molecular oxygen or oxygen radicals [Eqs. (3)–(5)]:

$$CH_4+O_2 \rightleftharpoons CH_3^{\bullet}+HO_2^{\bullet} \tag{3}$$

$$CH_4+O_2 \rightleftharpoons CH_3O^{\bullet}+OH^{\bullet} \tag{4}$$

$$CH_4+O^{\bullet} \rightleftharpoons CH_3^{\bullet}+OH^{\bullet} \tag{5}$$

in which $HO_2^{\bullet}$ can further contribute to the methane activation as [Eq. (6)]:

$$CH_4+HO_2^{\bullet} \rightleftharpoons CH_3^{\bullet}+H_2O_2 \tag{6}$$

Nonoxidative $CH_3^{\bullet}$ production may proceed by either thermal cracking or $H^{\bullet}$ radical attack as [Eqs. (7) and (8)]:

$$CH_4 \rightleftharpoons CH_3^{\bullet}+H^{\bullet} \tag{7}$$

$$CH_4+H^{\bullet} \rightleftharpoons CH_3^{\bullet}+H_2 \tag{8}$$

both of which require high temperatures.[4]

The heterogeneous pathway for $CH_3^{\bullet}$ radical formation is initiated by the reaction with surface-adsorbed oxygen O(s) [Eq. (9)]:[28,29]

$$CH_4+O(s) \rightleftharpoons CH_3^{\bullet}+OH(s) \tag{9}$$

As the O—H bonds in H_2O ($497\ kJ\,mol^{-1}$) are stronger than the C—H bond in CH_4 ($439\ kJ\,mol^{-1}$), methane activation can also be accomplished by the reaction of CH_4 with $OH^{\bullet}$ radicals as [Eq. (10)]:[4,33–37]

$$CH_4+OH^{\bullet} \rightleftharpoons CH_3^{\bullet}+H_2O \tag{10}$$

In addition to Reactions (4) and (5), Takanabe and Iglesia[38] proposed that $OH^{\bullet}$ radicals can be produced by the reaction of H_2O with O(s) on the surface or O_2 in the gas phase as [Eqs. (11) and (12)]:

$$H_2O+O(s) \rightleftharpoons OH^{\bullet}+OH(s) \tag{11}$$

$$2\,H_2O+O_2 \rightleftharpoons 4\,OH^{\bullet} \tag{12}$$
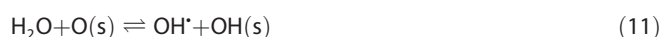
In the presence of a catalyst, Reaction (11) is likely the dominant pathway.

Following methyl radical formation as a result of CH_4 activation, $CH_3^{\bullet}$ recombination in the gas-phase produces C_2H_6 directly by a three-body reaction as [Eq. (13)]:

$$CH_3^{\bullet}+CH_3^{\bullet}+M \rightarrow C_2H_6+M \tag{13}$$

Further C_2H_6 dehydrogenation produces C_2H_4 by reaction with $H^{\bullet}$, $OH^{\bullet}$, or $CH_3^{\bullet}$ to form the ethyl radical ($C_2H_5^{\bullet}$). Reactions with O(s) can also produce the ethyl radical ($C_2H_5^{\bullet}$) that also leads to C_2H_4.

Lundsford argued that CO is formed by gas-phase reactions, whereas H_2O and CO_2 are formed by surface reactions.[39] Sun et al.[28] proposed that CO, CO_2, and H_2O are formed both by homogeneous and heterogeneous pathways.

Broadly speaking, the reaction pathways are expected to be generally similar for Li/MgO, Sr/CaO, Sr/La_2O_3, $Mn/Na_2WO_4/SiO_2$, $Mn/Na_2WO_4/MgO$, and La_2O_3/CeO_2 catalysts.[10,12,24,26,39]

2.2. Gas-phase kinetics

Based on extensive combustion research, the elementary gas-phase reactions that contribute to the OCM process are relatively well understood. Several gas-phase reaction mechanisms have proposed since the early 1980s,[4,33–36,40–45] most of which are concerned primarily with methane total oxidation. The gas-phase kinetic models by Warnatz,[34] Mims et al.,[42] Smith et al.,[35] Wang et al.,[43] and Dooley et al.[36] contain comprehensive reaction steps for the oxidation of C_1–C_4 species. The gas-phase mechanisms developed by Zanthoff and Baerns,[41] Lopez et al.,[44] and Chen et al.[33] were developed specifically for the oxidation of C_1–C_3 species. The mechanism described by Konov[45] is concerned with C_1–C_6 species and their nitrates formed in N-containing environments. Some of these reaction mechanisms contain thousands of reaction steps among hundreds of species. However, such detailed mechanisms can be computationally expensive. The resolution of concentration profiles with thousands of reaction steps is usually practical for 1D physical models. Nevertheless, the development of reaction mechanisms with fewer species and reactions has a significant practical value.

The reduced gas-phase kinetic models by Zanthoff and Baerns,[41] Reyes et al.,[4] and Chen et al.[33] were developed and validated for OCM conditions. The model described by Zanthoff and Baerns[41] is composed of 193 reversible elementary gas-phase reaction steps between 33 species. The model developed by Reyes et al.[4] contains 145 reversible gas-phase reaction step between 28 species. The model constructed by Chen et al.[33] is smaller and contains 39 reversible gas-phase reactions among 22 species. As each of these reduced mechanisms was developed and validated under different reaction conditions (e.g., residence time, CH_4/O_2 ratios, temperature range), the gas-phase behaviors may not be captured fully for different conditions.

In 1994, with the use of a tubular packed-bed reactor with a Ce/Li/MgO OCM catalyst, Dittmeyer measured temperature and concentration profiles.[46] With measurements and comparisons of profiles with and without the catalyst, this study provided new insights about the interactions of gas-phase species and catalytic chemistry. More recently, Mavlyankariev studied OCM gas-phase chemistry numerically and experimentally.[47] The gas-phase concentration and temperature profiles along an empty tubular reactor were measured by using a microprobe sampling technique developed originally by Horn et al.[48] Mavlyankariev also tested all available kinetic models[4,33–36,41–45] and compared them with the experimental measurements. Mavlyankariev reported that the kinetic model proposed by Dooley et al.,[36] which contained 1583 elementary reactions between 269 species, delivered the best performance to predict the concentration and temperature profiles within the reactor. Mavlyankariev then reduced the model put forward by Dooley et al.[36] to a mechanism with 332 reaction steps and 50 species. Mavlyankariev also reported that the model developed by Chen et al.[33] predicted much less conversion than was measured.

Despite the deficiencies identified by Mavlyankariev, the relatively small model presented by Chen et al.[33] does represent all the major and minor OCM products. In part because of its compact size, the coupling of the model described by Chen et al. with surface-chemistry models is relatively straightforward. The present model begins with the gas-phase model developed by Chen et al.,[33] but we modified the pre-exponential rate constants based on the modeling of the spatially resolved concentration and temperature profiles measured by Zohour et al.[49]

2.3. Proposed gas-phase OCM chemistry

The 39 elementary gas-phase reaction steps for the OCM process proposed by Chen et al.,[28,33] which involves 12 stable molecules and 10 radicals, are listed in Table 2. The 12 molecules are O_2, H_2O, CO, CO_2, CH_4, CH_2O, C_2H_2, C_2H_4, C_2H_6, C_3H_6,

Table 2. Gas-phase OCM reaction mechanism. The reaction pathways are based on those reported by Chen et al..[33] The rate-expression parameters are represented in Arrhenius form as $k = AT^\beta exp(-E/RT)$.

	Reaction	A [cm, mol, s]	β –	E [kJ mol^{-1}]
1.	$CH_4 + O_2 \rightleftarrows CH_3^\bullet + HO_2^\bullet$	$1.83 \times 10^{+12}$	0.00	193.86
2.	$CH_4 + H^\bullet \rightleftarrows CH_3^\bullet + H_2$	$2.04 \times 10^{+14}$	0.00	41.17
3.	$CH_4 + O^\bullet \rightleftarrows CH_3^\bullet + OH^\bullet$	$9.27 \times 10^{+14}$	0.00	33.83
4.	$CH_4 + OH^\bullet \rightleftarrows CH_3^\bullet + H_2O$	$5.43 \times 10^{+17}$	0.00	71.43
5.	$CH_4 + HO_2^\bullet \rightleftarrows CH_3^\bullet + H_2O_2$	$3.01 \times 10^{+13}$	0.00	59.61
6.	$CH_3^\bullet + O_2 \rightleftarrows CH_3O^\bullet + O^\bullet$	$1.58 \times 10^{+14}$	0.00	91.00
7.	$CH_3^\bullet + O_2 \rightleftarrows CH_2O^\bullet + OH^\bullet$	$8.59 \times 10^{+13}$	0.00	73.66
8.	$CH_3^\bullet + HO_2^\bullet \rightleftarrows CH_3O^\bullet + OH^\bullet$	$4.85 \times 10^{+14}$	0.00	0.00
9.	$CH_3^\bullet + CH_3^\bullet + M \rightleftarrows C_2H_6 + M$	$2.00 \times 10^{+19}$	0.00	0.00
10.	$CH_3O^\bullet + M \rightleftarrows CH_2O^\bullet + H + M$	$3.58 \times 10^{+20}$	0.00	35.0
11.	$CH_2O^\bullet + OH^\bullet \rightleftarrows CHO^\bullet + H_2O$	$9.80 \times 10^{+12}$	0.00	5.00
12.	$CH_2O^\bullet + HO_2^\bullet \rightleftarrows CHO^\bullet + H_2O_2$	$9.17 \times 10^{+14}$	0.00	10.12
13.	$CH_2O^\bullet + CH_3^\bullet \rightleftarrows CHO^\bullet + CH_4$	$1.00 \times 10^{+13}$	0.00	95.03
14.	$CHO^\bullet + M \rightleftarrows CO + H^\bullet + M$	$3.80 \times 10^{+12}$	0.00	64.36
15.	$CHO^\bullet + O_2 \rightleftarrows CO + HO_2^\bullet$	$9.71 \times 10^{+16}$	0.00	0.00
16.	$CO + HO_2^\bullet \rightleftarrows CO_2 + OH^\bullet$	$3.08 \times 10^{+16}$	0.00	107.34
17.	$C_2H_6 + H^\bullet \rightleftarrows C_2H_5^\bullet + H_2$	$8.10 \times 10^{+09}$	0.00	51.70
18.	$C_2H_6 + OH^\bullet \rightleftarrows C_2H_5^\bullet + H_2O$	$8.45 \times 10^{+12}$	0.00	17.16
19.	$C_2H_6 + CH_3^\bullet \rightleftarrows C_2H_5^\bullet + CH_4$	$8.29 \times 10^{+13}$	0.00	64.73
20.	$C_2H_5^\bullet + HO_2^\bullet \rightleftarrows CH_3^\bullet + CH_2O^\bullet + OH^\bullet$	$8.48 \times 10^{+13}$	0.00	0.0
21.	$C_2H_5^\bullet + M \rightleftarrows C_2H_4 + H^\bullet + M$	$3.96 \times 10^{+23}$	0.00	167.66
22.	$C_2H_5^\bullet + O_2 \rightleftarrows C_2H_4 + HO_2^\bullet$	$5.35 \times 10^{+12}$	0.00	53.20
23.	$C_2H_4 + O_2 \rightleftarrows C_2H_3^\bullet + HO_2^\bullet$	$9.81 \times 10^{+13}$	0.00	144.55
24.	$C_2H_4 + H^\bullet \rightleftarrows C_2H_3^\bullet + H_2$	$1.50 \times 10^{+10}$	0.00	42.70
25.	$C_2H_4 + OH^\bullet \rightleftarrows C_2H_3^\bullet + H_2O$	$6.12 \times 10^{+11}$	0.00	24.70
26.	$C_2H_4 + CH_3^\bullet \rightleftarrows C_2H_3^\bullet + CH_4$	$3.99 \times 10^{+12}$	0.00	51.46
27.	$C_2H_4 + OH^\bullet \rightleftarrows CH_3^\bullet + CH_2O^\bullet$	$2.72 \times 10^{+11}$	0.00	0.00
28.	$C_2H_3^\bullet + M \rightleftarrows C_2H_2 + H^\bullet + M$	$4.21 \times 10^{+16}$	0.00	176.44
29.	$C_2H_3^\bullet + O_2 \rightleftarrows C_2H_2 + HO_2^\bullet$	$9.00 \times 10^{+12}$	0.00	0.00
30.	$C_2H_3^\bullet + O_2 \rightleftarrows CH_2O^\bullet + CHO^\bullet$	$9.50 \times 10^{+17}$	0.00	0.00
31.	$C_2H_5^\bullet + CH_3^\bullet \rightleftarrows C_3H_8$	$6.00 \times 10^{+13}$	0.00	0.00
32.	$C_3H_8 + H^\bullet \rightleftarrows C_3H_7^\bullet + H_2$	$7.00 \times 10^{+09}$	0.00	32.0
33.	$C_2H_4 + CH_3^\bullet \rightleftarrows C_3H_7^\bullet$	$8.00 \times 10^{+12}$	0.00	29.00
34.	$C_3H_7^\bullet \rightleftarrows C_3H_6 + H^\bullet$	$5.50 \times 10^{+15}$	0.00	156.00
35.	$O_2 + H^\bullet \rightleftarrows OH^\bullet + O^\bullet$	$2.20 \times 10^{+14}$	0.00	70.30
36.	$O_2 + H^\bullet + M \rightleftarrows HO_2^\bullet + M$	$1.39 \times 10^{+17}$	0.00	0.0
37.	$HO_2^\bullet + HO_2^\bullet \rightleftarrows O_2 + OH^\bullet + OH^\bullet$	$8.00 \times 10^{+13}$	0.00	0.00
38.	$H_2O_2 + M \rightleftarrows OH^\bullet + OH^\bullet + M$	$1.27 \times 10^{+18}$	0.00	169.36

and H_2O_2. The 11 radical species are $H^\bullet$, $O^\bullet$, $OH^\bullet$, $HO_2^\bullet$, $CH_3^\bullet$, $HCO^\bullet$, $CHO^\bullet$, $CH_3O^\bullet$, $C_2H_5^\bullet$, $C_2H_7^\bullet$, and $C_3H_3^\bullet$. The gas-phase species may react between themselves or, as discussed subsequently, may react with surface-adsorbed species on the catalyst.

According to the mechanism put forward by Chen et al.,[33] methane activation is initiated by direct reactions with O_2 and the radicals $O^\bullet$, $H^\bullet$, $OH^\bullet$, and $HO_2^\bullet$. $CH_3^\bullet$ recombination first produces C_2H_6. Subsequent radical attack ($H^\bullet$, $OH^\bullet$, or $CH_3^\bullet$) on C_2H_6 promotes dehydrogenation to form gas-phase H_2, H_2O, CH_4, and the unstable $C_2H_5^\bullet$ radical. The desired C_2H_4 is produced by the further reactions of $C_2H_5^\bullet$ with radicals ($H^\bullet$, $O^\bullet$, and $OH^\bullet$) and O_2. Unfortunately, the rich gas-phase radical pool promotes further deep oxidation of C_2H_4 to form CO_x and H_2O. Higher hydrocarbons such as C_3 species are also formed through $C_2H_5^\bullet$ and $CH_3^\bullet$ radical–radical reactions.

All the reaction steps in Table 2 are written reversibly, and the reverse reaction rates are evaluated based on the reaction

equilibrium constants. The GRI thermodynamic database is used as the source of the thermodynamic properties of the species. The Arrhenius rate-expression parameters listed in Table 2 are modified from those reported by Chen et al.[33]

Based on the adjusted rate constants, the overall methane conversion is controlled primarily by methane activation reactions (i.e., Table 2, Reactions 1 and 2). The $CH_3^{\cdot}$ radical recombination reaction (Table 2, Reaction 9) also plays a significant role in the overall methane conversion. The CO and CO_2 concentrations depend strongly on the oxidation of $CH_3^{\cdot}$ radicals through Reactions 6 and 7 (Table 2). The formation of C_3 species is controlled by chain growth if the $CH_3^{\cdot}$ radical attacks C_2H_4 and $C_2H_5^{\cdot}$ (Reactions 31 and 33). The low-temperature CO_x formation is controlled by the gas-phase oxidation of formaldehyde (Table 2, Reaction 12).

2.4. Previous studies on OCM surface kinetics

Most previous studies on OCM surface kinetics focus on catalysts with relatively simple crystal structures, such as Li/MgO and La_2O_3. Simon et al.[50] proposed a detailed surface mechanism for La_2O_3, which is coupled with 450 gas-phase reactions. The model was validated using measured results from an isothermal, continuously stirred tank reactor. Unfortunately, they did not describe the gas-phase reaction mechanism fully.

Sinev et al.[51–53] developed a detailed surface reaction mechanism for the OCM process on Li/MgO catalysts. They reported that lattice oxygen in Li/MgO could participate in the catalytic process. They considered three Li oxidation states (Li, LiO, and LiOH) and their reactions with gas-phase species. Subsequently, the surface kinetic model was extended to predict newer OCM experiments.[54, 55]

Sun et al.[28] proposed a detailed OCM reaction mechanism for Li/MgO and Sn/Li/MgO catalysts. This mechanism consisted of 14 surface reactions and 39 gas-phase reactions. The mechanism represents the adsorption of gas-phase species, reaction of gas-phase species (either radical or stable molecules) with surface adsorbates (Eley–Rideal steps), and surface–surface reactions. Methane activation proceeds by methyl radical formation in the gas-phase as well as on the catalyst surface. Methyl radicals recombine to form C_2H_6. The kinetic model also includes the direct oxidation of CH_4 to form CO_x but does not consider the deep oxidation of C_2H_4 by surface reactions.

Alexiadis et al.[31] extended the reaction network by including the deep oxidation of C_2H_4 by surface reactions. The reaction kinetics were then applied to several other catalysts, which included Mn/Na_2WO_4/SiO_2, Li/MgO, SrLaO, and Sn/LiMgO.[32, 56] The activation barriers of key reaction families (i.e., $H^{\cdot}$ abstraction, $OH^{\cdot}$ recombination, CO oxidation, and C–C cleavage on the surface) on different catalysts were adjusted based on the Evans–Polanyi relationship, that is, $E_a = E_0 + \alpha \Delta H$, in which E_a is the forward activation barrier, E_0 is a reference activation energy, ΔH is the reaction enthalpy, and $0 \le \alpha \le 1$. Both E_0 and α are specific to the reaction family and the catalyst.[56]

Instead of focusing on an individual catalyst and reaction rate constants, Su et al.[57] used microkinetic modeling to predict the upper limit of the C_2 yield. From a plausible OCM reaction pathway and using the gas-phase kinetics described by Mims et al.,[42] the maximum C_2 yield can be reached by maximizing the significant reaction rates. The OCM process was found to be a thermodynamically limited process with an upper limit for the C_2 yield of 28%.

2.5. Proposed surface reaction mechanism

In the present study, we begin with the surface reaction pathways proposed by Alexiadis et al.,[31] which were developed originally for the OCM process on Li/MgO and Sn/Li/MgO catalysts. The reaction network includes reactions between gas-phase and surface-adsorbed species. The reactions are stated typically in terms of Eley–Rideal or Langmuir–Hinshelwood formalisms. The activation of CH_4 with O(s) produces $CH_3^{\cdot}$, which promotes the desired C_2 production. However, O(s) can also react competitively with $CH_3^{\cdot}$ radicals to form undesired CO and CO_2. The desired gas-phase products C_2H_4 and C_2H_6 can also react with O(s) to form $C_2H_5^{\cdot}$ and $C_2H_3^{\cdot}$, which can further react in the gas phase to promote undesired CO, CO_2, and H_2O. As anticipated, the relatively complex heterogeneous reaction pathways that lead to C_{2+} formation are influenced significantly by temperature, residence time, and catalyst loading.

The CeO_2 in the La_2O_3/CeO_2 may play a role as a redox-active catalyst support, which may help to diminish coke formation and thus improve the catalyst durability. In other words, the La_2O_3/CeO_2 structure may exhibit some bifunctional catalytic behaviors. However, the current reaction mechanism does not consider any such catalyst bifunctionality. Rather, it approximates the La_2O_3/CeO_2 as a single-phase surface. The nomenclature La(s) is used to represent a surface site. The effective catalyst site density (Γ) is estimated to be 9.84×10^{-10} mol cm^{-2}.

The heterogeneous reaction mechanism and rate expressions are given in Table 3. The reaction mechanism involves 11 surface species and 16 gas-phase species, all of which participate in gas-phase reactions as well. The surface reaction mechanism is written as irreversible reaction pairs with pre-exponential factors, temperature dependencies, and activation energies represented in modified Arrhenius form or as sticking probabilities. Writing the reactions as irreversible pairs avoids the need to know the thermodynamic properties of surface adsorbents. However, the reaction pairs are not constrained to be thermodynamically consistent and preserve microscopic reversibility. A possible consequence of the irreversible-pair formulation is that the de facto equilibrium constants (i.e., ratio of forward and reverse rates) may appear to be nonphysical. For example, an artificially high equilibrium constant simply means that the forward reaction is dominant. Such behavior has no practical consequence on the model predictions but could potentially cause computational difficulties. Nevertheless, the gas-phase reactions are reversible and thermodynamically consistent, which does preserve overall thermodynamic consistency for the gas-phase species. Details of the surface-chemistry formalism have been given by Kee et al.[58] and Coltrin et al.[59]

Table 3. Surface reaction kinetics for oxidative coupling of methane over La_2O_3/CeO_2 nanofabric catalysts. Gas-phase radical species are indicated by the $^\bullet$. The active site is shown as La(s) and the catalytic surface site density is $\Gamma = 9.84 \times 10^{-10}$ mol cm^{-2}.

	Reaction	A or sticking coefficient [cm, mol, s]	β –	E [kJ mol⁻¹]
1.	$O_2 + La(s) \rightarrow O(s) + O(s)$	1.80×10^{-01}	0.00	0.00[a]
2.	$O(s) + O(s) \rightarrow O_2 + La(s) + La(s)$	$1.00 \times 10^{+22}$	0.00	60.7
3.	$CH_4 + O(s) \rightarrow CH_3^\bullet + OH(s)$	$7.50 \times 10^{+10}$	0.00	174.4
4.	$CH_3^\bullet + OH(s) \rightarrow CH_4 + O(s)$	$1.91 \times 10^{+10}$	0.00	105.0
5.	$C_2H_4 + O(s) \rightarrow C_2H_3^\bullet + OH(s)$	$6.40 \times 10^{+10}$	0.00	100.4
6.	$C_2H_3^\bullet + OH(s) \rightarrow C_2H_4 + O(s)$	$5.42 \times 10^{+13}$	0.00	90.1
7.	$C_2H_6 + O(s) \rightarrow C_2H_5^\bullet + OH(s)$	$4.05 \times 10^{+13}$	0.00	88.2
8.	$C_2H_5^\bullet + OH(s) \rightarrow C_2H_6 + O(s)$	$6.37 \times 10^{+12}$	0.00	98.5
9.	$OH(s) + OH(s) \rightarrow H_2O(s) + O(s)$	$7.25 \times 10^{+20}$	0.00	190.3
10.	$H_2O(s) + O(s) \rightarrow OH(s) + OH(s)$	$1.17 \times 10^{+10}$	0.00	138.2
11.	$H_2O(s) \rightarrow H_2O + La(s)$	$1.10 \times 10^{+13}$	0.00	54.2
12.	$H_2O + La(s) \rightarrow H_2O(s)$	3.52×10^{-02}	0.00	0.00[a]
13.	$CH_3^\bullet + O(s) \rightarrow CH_3O(s)$	$7.25 \times 10^{+10}$	0.00	0.0
14.	$CH_3O(s) \rightarrow CH_3^\bullet + O(s)$	$2.24 \times 10^{+11}$	0.00	144.6
15.	$CH_3O(s) + O(s) \rightarrow CH_2O(s) + OH(s)$	$9.72 \times 10^{+22}$	0.00	0.0
16.	$CH_2O(s) + OH(s) \rightarrow CH_3O(s) + O(s)$	$1.69 \times 10^{+21}$	0.00	145.9
17.	$CH_2O(s) + O(s) \rightarrow HCO(s) + OH(s)$	$9.69 \times 10^{+20}$	0.00	55.1
18.	$HCO(s) + OH(s) \rightarrow CH_2O(s) + O(s)$	$1.75 \times 10^{+20}$	0.00	132.6
19.	$HCO(s) + O(s) \rightarrow CO(s) + OH(s)$	$9.72 \times 10^{+24}$	0.00	5.7
20.	$CO(s) + OH(s) \rightarrow HCO(s) + O(s)$	$1.81 \times 10^{+19}$	0.00	133.9
21.	$CO(s) + O(s) \rightarrow CO_2(s) + La(s)$	$5.91 \times 10^{+22}$	0.00	0.0
22.	$CO_2(s) + La(s) \rightarrow CO(s) + O(s)$	$2.39 \times 10^{+20}$	0.00	155.3
23.	$CO + La(s) \rightarrow CO(s)$	5.00×10^{-06}	0.00	0.0[a]
24.	$CO(s) \rightarrow CO + La(s)$	$3.81 \times 10^{+14}$	0.00	45.4
25.	$CO_2 + La(s) \rightarrow CO_2(s)$	2.50×10^{-06}	0.00	0.00[a]
26.	$CO_2(s) \rightarrow CO_2 + La(s)$	$5.80 \times 10^{+14}$	0.00	45.9
27.	$C_2H_4 + O(s) \rightarrow C_2H_4O(s)$	$2.20 \times 10^{+12}$	0.00	85.3
28.	$C_2H_4O(s) \rightarrow C_2H_4 + O(s)$	$6.00 \times 10^{+11}$	0.00	186.3
29.	$C_2H_4O(s) + O(s) \rightarrow C_2H_3O(s) + OH(s)$	$1.00 \times 10^{+21}$	0.00	76.00
30.	$C_2H_3O(s) + OH(s) \rightarrow C_2H_4O(s) + O(s)$	$1.00 \times 10^{+21}$	0.00	3.0
31.	$C_2H_3O(s) + O(s) \rightarrow CH_2O(s) + HCO(s)$	$1.00 \times 10^{+21}$	0.00	69.0
32.	$CH_2O(s) + HCO(s) \rightarrow C_2H_3O(s) + O(s)$	$1.00 \times 10^{+21}$	0.00	186.5
33.	$C_2H_5^\bullet + O(s) \rightarrow C_2H_4 + OH(s)$	$1.00 \times 10^{+12}$	0.00	183.5
34.	$C_2H_4 + OH(s) \rightarrow C_2H_5^\bullet + O(s)$	$8.00 \times 10^{+10}$	0.00	70.9
35.	$CH_3O^\bullet + O(s) \rightarrow CH_2O^\bullet + OH(s)$	$7.00 \times 10^{+11}$	0.00	307.8
36.	$CH_2O^\bullet + OH(s) \rightarrow CH_3O^\bullet + O(s)$	$1.00 \times 10^{+11}$	0.00	26.5
37.	$CH_2O^\bullet + O(s) \rightarrow CHO^\bullet + OH(s)$	$1.00 \times 10^{+13}$	0.00	109.9
38.	$CHO^\bullet + OH(s) \rightarrow CH_2O^\bullet + O(s)$	$1.00 \times 10^{+10}$	0.00	39.3
39.	$CHO^\bullet + O(s) \rightarrow CO + OH(s)$	$1.00 \times 10^{+12}$	0.00	88.1
40.	$CO + OH(s) \rightarrow CHO^\bullet + O(s)$	$1.00 \times 10^{+13}$	0.00	89.7
41.	$H_2 + O(s) \rightarrow H^\bullet + OH(s)$	$8.00 \times 10^{+13}$	0.00	400.0
42.	$H^\bullet + OH(s) \rightarrow H_2 + O(s)$	$1.00 \times 10^{+10}$	0.00	0.0
43.	$H_2O_2 + O(s) \rightarrow HO_2^\bullet + OH(s)$	$1.00 \times 10^{+13}$	0.00	344.0
44.	$HO_2^\bullet + OH(s) \rightarrow H_2O_2 + O(s)$	$1.00 \times 10^{+13}$	0.00	13.8
45.	$OH^\bullet + O(s) \rightarrow O^\bullet + OH(s)$	$1.00 \times 10^{+11}$	0.00	390.0
46.	$O^\bullet + OH(s) \rightarrow OH^\bullet + O(s)$	$1.00 \times 10^{+11}$	0.00	0.0
47.	$H_2O + O(s) \rightarrow OH^\bullet + OH(s)$	$1.00 \times 10^{+11}$	0.00	460.0
48.	$OH^\bullet + OH(s) \rightarrow H_2O + O(s)$	$1.00 \times 10^{+11}$	0.00	0.0
49.	$HO_2^\bullet + O(s) \rightarrow O_2 + OH(s)$	$1.00 \times 10^{+11}$	0.00	224.0
50.	$O_2 + OH(s) \rightarrow HO_2^\bullet + O(s)$	$1.00 \times 10^{+13}$	0.00	54.0
51.	$HO_2^\bullet + La(s) \rightarrow OH^\bullet + O(s)$	$1.00 \times 10^{+10}$	0.00	0.0
52.	$OH^\bullet + O(s) \rightarrow HO_2^\bullet + La(s)$	$1.00 \times 10^{+11}$	0.00	30.0

[a] Most reaction rate expressions are written in modified Arrhenius form $k = AT^\beta exp(-E/RT)$. Reactions 1, 12, 23 and 25 are the adsorption reactions and A represents the sticking coefficient.

The nominal values for the rate constants are estimated using transition-state theory. Pre-exponential factors A are evaluated as [Eq. (14)]:

$$A = \frac{k_B T}{h} \frac{1}{\Gamma^{n-1}} \qquad (14)$$

in which k_B is the Boltzmann constant, h is the Planck constant, Γ is the surface site density, and n is the reaction order. For a first-order surface reaction, the nominal value of A is estimated to be approximately 10^{13} s^{-1}.[60,61]

The initial activation barriers are estimated based on the Evans–Polanyi relationship between reaction enthalpies and activation barriers. The reaction enthalpies for H abstraction from CH_4, OH recombination, CO oxidation and C—C cleavage, and O_2 chemisorption on the surface are used as catalyst descriptors.[32] The reaction rates (i.e., activation barriers, temperature dependencies, and pre-exponential factors) were adjusted to match the spatially resolved concentration and temperature profile measurements reported by Zohour et al.[49] The "fitting" process did not use any formal or automated optimization procedure. Rather, it was accomplished by extensive packed-bed-reactor simulations and careful comparisons with the measured profiles.

3. Packed-bed profile measurements

We use spatially resolved measurements that were published previously by Zohour et al.[49,62] A flakelike fabric "particle" of the La_2O_3/CeO_2 nanofiber catalyst is shown in Figure 1a, and a SEM image that shows the small-scale nanofiber structure clearly is presented in Figure 1b. The effective bed porosity is estimated to be 60%.

A schematic representation of the packed-bed reactor with microprobe sampling is shown in Figure 2. The quartz tube that houses the catalyst bed has an internal diameter of 4 mm. The tube was packed with 20 mg of the La_2O_3/CeO_2 nanofiber catalyst sandwiched between two quartz wool layers in front of and behind the catalyst. The catalyst bed was 14 mm long. The front-side quartz wool was 4 mm long, and the back-end quartz wool was 7 mm long. The reactor was housed in a furnace heated electrically, and the furnace temperature was set to be the same as the gas temperature of the premixed CH_4 and O_2 feed flow. The total inlet flow rate was fixed as 160 cm^3 min^{-1} at standard temperature and pressure (STP). In a series of experiments, the premixed CH_4/O_2 ratio was varied from 7 to 11 without the addition of any diluent. The inlet gas temperature varied from 570 to 700 °C.

An 800 µm quartz capillary probe was positioned along the centerline of the packed bed for gas sampling. The microprobe axial position was controlled manually by using a micropositioning device. The capillary probe withdrew gas samples at 5 cm^3 min^{-1} at STP, and the gas was analyzed by using GC. Steady-state concentrations of CH_4, O_2, H_2,
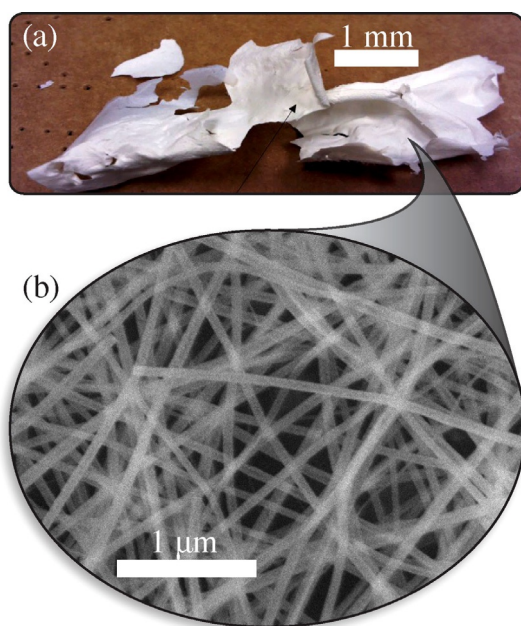
Figure 1. a) Two fabric flakes of the La_2O_3/CeO_2 nanofabric catalyst. b) SEM image of the nanofiber structure.
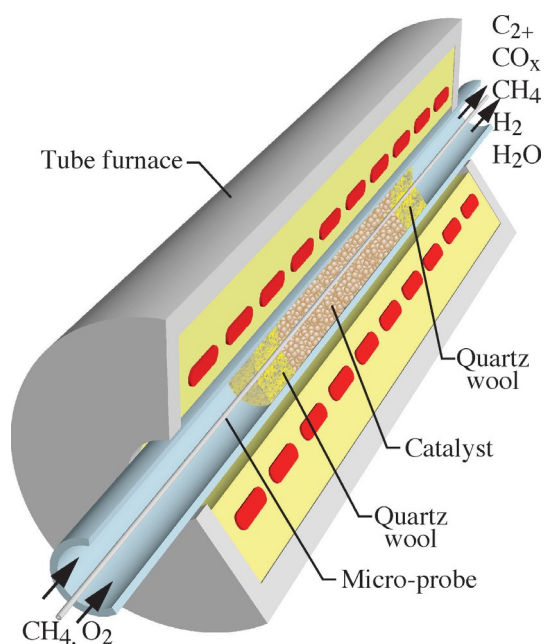
Figure 2. Schematic representation of the reactor bed. The 14 mm catalyst section is held in place by quartz wool. The internal tube diameter is 4 mm. The translating sampling probe is positioned along the bed centerline.

CO, CO_2, C_2H_4, C_2H_6, and C_3 (C_3H_6 and C_3H_8) were measured directly by using GC, and the local H_2O concentration was evaluated from an oxygen atom balance. The quartz capillary probe also held a K-type thermocouple. After gas sampling, the temperature measurement was accomplished when no gas was withdrawn by the capillary tube. The measured temperature and concentration profile began at the front face of the quartz wool, continued through the catalyst bed, and through the

back side quartz wool. Thus, concentration and temperature measurements were made within the entire 25 mm length of the packed bed.

4. Packed-bed model

The tubular packed-bed reactor was modeled by assuming a 1 D axial reacting porous medium. In other words, any radial variations were neglected. As the catalytic packed-bed model has been documented previously,[63] only a summary is provided here.

The transient continuity equations for gas-phase species and overall mass conservation can be written in a conservative form as [Eqs. (15) and (16)]:

$$\frac{\partial(\varphi_g \rho_g Y_k)}{\partial t} + \nabla \cdot \mathbf{j}_k = (\varphi_g \dot{\omega}_k + A_s \dot{s}_k) W_k \qquad (15)$$

$$\frac{\partial(\varphi_g \rho_g)}{\partial t} + \sum_{k=1}^{K_g} \nabla \cdot \mathbf{j}_k = \sum_{k=1}^{K_g} A_s \dot{s}_k W_k \qquad (16)$$

In these equations, the independent variables are t and the axial spatial coordinate. Dependent variables are ρ_g and Y_k, which represent the gas-phase mixture mass density and the species mass fractions. Other variables and parameters include the bed porosity ϕ_g and the specific catalyst surface area A_s. The species molecular weights are represented as W_k. Chemical production rates by homogeneous and heterogeneous reactions are represented by $\dot{\omega}_k$ and $\dot{s}_k$, respectively. The total number of gas-phase species is represented by K_g.

If we consider the molecular diffusion (ordinary and Knudsen) and Darcy flow for the gaseous species transport within the porous bed, the gas-phase mass fluxes $\mathbf{j}_k$ can be represented as [Eq. (17)]:

$$\mathbf{j}_k = \rho_g Y_k \mathbf{v} - W_k D_k^e \nabla[X_k] \qquad (17)$$

The superficial velocity $\mathbf{v}$ thorough the porous media can be represented using Darcy's law as [Eq. (18)]:

$$\mathbf{v} = -\frac{B}{\mu} \nabla p \qquad (18)$$

in which B is the permeability of the porous medium, p is the gas-phase pressure, and μ is the gas-phase mixture viscosity. An effective diffusion coefficient D_k^e can be expressed in terms of ordinary and Knudsen diffusion as [Eq. (19)]:

$$\frac{1}{D_k^e} = \frac{1}{D_{k,m}^e} + \frac{1}{D_{k,Kn}^e} \qquad (19)$$

The effective ordinary and Knudsen diffusion coefficients are written as [Eq. (20)]:

$$D_{k,m}^e = \frac{\varphi_g}{\tau} D_{k,m}$$

$$D_{k,Kn}^e = \frac{2}{3} \frac{r_p \varphi_g}{\tau} \sqrt{\frac{8RT}{\pi W_k}}$$

(20)

The effective ordinary mixture-averaged diffusion coefficient is $D_{k,m}^e$, and $D_{k,m}$ is the gas-phase mixture-averaged diffusion coefficient. The effective Knudsen diffusion is represented as $D_{k,Kn}^e$. The effective pore radius is denoted as r_p, and the tortuosity is represented as τ. All the other thermodynamic properties and transport parameters were evaluated using the Chemkin software, and fundamental details of the underpinning formulations have been described by Kee et al.[58]

In addition to gas-phase concentrations, the heterogeneous reaction rates (Table 3) depend also on the concentrations of the surface adsorbates. The adsorbate concentrations on the catalyst surface can be represented using site fractions θ_k. If we neglect any adsorbate diffusion on the catalyst surfaces, the governing equations for temporal variations of surface species caused by heterogeneous reactions can be represented as [Eq. (21)]:

$$\frac{d\theta_k}{dt} = \frac{\dot{s}_k}{\Gamma}$$

(21)

in which Γ is the available site density. At steady state $\dot{s}_k = 0$ for all the adsorbed surface species.

An energy-conservation equation could be used to predict the thermal profiles within the bed. However, rather than solving an energy equation, the present model imposes the measured axial temperature profile. This approach enables attention to be focused on the reaction mechanisms without inevitable assumptions about thermal coupling with the furnace.

Solving the conservation equations depends on boundary conditions. At the reactor inlet, the species mass flow rates are specified. The pressure at the outlet is also specified. The spatial operators are approximated using 1D finite-volume spatial discretization on a mesh network. The transient model is solved using a method-of-lines algorithm, and the time marching was accomplished by using Limex.[64] The steady-state profiles are found as the long-time solution of the transient problem.

The overall reactor performance can be represented in terms of reactant (i.e., CH_4) conversion as well as product yields and selectivities. Within the bed, the local methane conversion can be defined as [Eq. (22)]:

$$X_{CH_4} = \frac{J_{CH_4,in} - J_{CH_4}}{J_{CH_4,in}}$$

(22)

in which $J_{CH_4,in}$ is the CH_4 molar flux at the reactor inlet, and J_{CH_4} is the local CH_4 molar flux. The species yields Y_k can be defined as [Eq. (23)]:

$$Y_k = \frac{n_{c,k} J_k}{J_{CH_4,in}}$$

(23)

in which $n_{c,k}$ is the number of carbon atoms in a particular species (e.g., $n_{c,C_2H_4} = 2$) and J_k is the local species molar flux, which can be related to the species mass fluxes j_k as $J_k = j_k/W_k$. The carbon selectivity S_k for a particular gas-phase species k can be defined as [Eq. (24)]:

$$S_k = \frac{n_{c,k} J_k}{J_{CH_4,in} - J_{CH_4}}$$

(24)

5. Results and Discussion

The physical parameters and operating conditions for the packed-bed reactor are given in Table 4. The packed-bed reactor model requires the physical parameters of the particle and packed-bed as model inputs. Unlike a typical packed-bed

**Table 4.** Reaction conditions used as model input parameters.

Parameter	Value
Inlet temperature, T	570–700 °C
Pressure, p	1 atm
Inlet velocity at STP, U_{in}	21.2 cm s^{-1}
CH_4/O_2 ratio	$7 \leq CH_4/O_2 \leq 11$
Catalyst bed length, L	14 mm
Reactor outer diameter	6 mm
Reactor inner diameter	4 mm
Bed porosity, ϕ	0.60
Tortuosity, τ	2.5
Surface-to-volume ratio, A_s	1.4×10^4 cm^{-1}
Quartz wool porosity	0.3
Quartz wool tortuosity	2.0
Quartz wool particle diameter	1.00×10^{-1} mm
Quartz wool pore diameter	9.00×10^{-2} mm

reactor, the catalyst is not in a particle form but rather in the form of packed flakelike sheets (Figure 1). Thus, typical parameters such as particle size and pore diameter have no direct physical meaning for the nanofiber structure. Nevertheless, particle size and pore diameter are estimated from the bulk density and packed-bed porosity by assuming spherical particles. The model uses a 125 μm particle diameter and 30 μm pore diameter as parameters.

The model considers three separate regions of the bed: the initial 4 mm quartz wool packing, the 14 mm catalyst bed, and the downstream 7 mm quartz wool packing. As gas-phase reactions can occur without a catalyst, it is important to represent the full reactor bed by considering the gas-phase reactions in both quartz wool sections. The reaction mechanism is calibrated and validated by the direct comparison of the predicted species mole fraction profiles, the methane conversion, and the product selectivity and yield with the experimental measurements for three different CH_4/O_2 ratios.

5.1. Effect of feed composition: $CH_4/O_2 = 9$

The concentration profiles of measured and predicted species for a feed mixture of $CH_4/O_2 = 9$ are shown in Figure 3. The
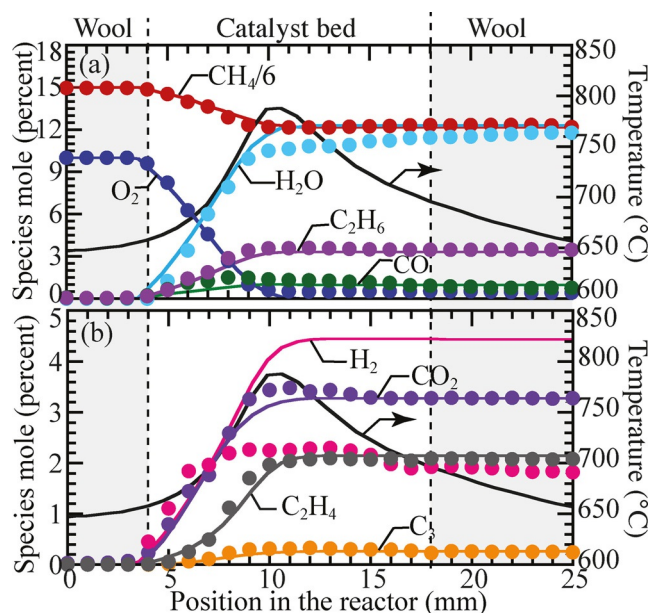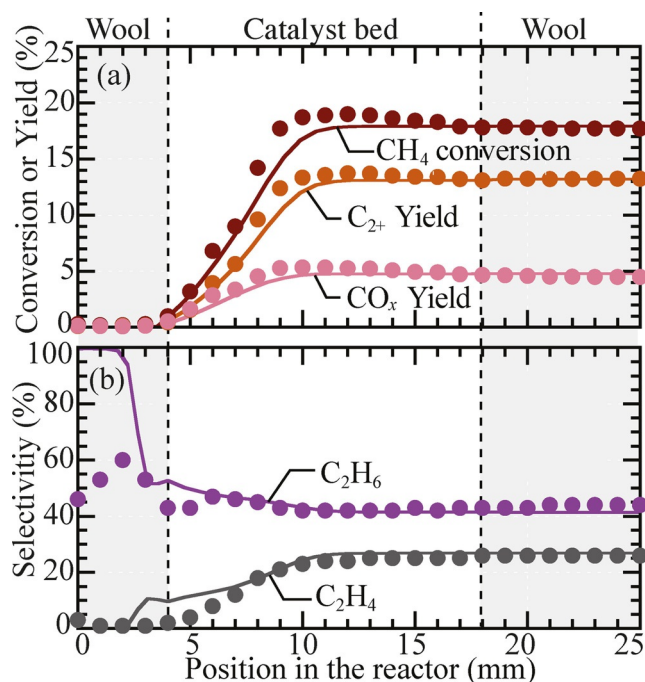
Figure 3. Comparison of measured (symbols) and predicted (lines) concentration and temperature profiles along the reactor bed. The reactor inlet temperature is 610 °C, the inlet CH_4 fraction is 0.90, and O_2 mole fraction is 0.10 ($CH_4/O_2 = 9$).


Figure 4. Comparison of measured (symbols) and predicted (lines) methane conversion and yield and C_2 selectivity along the reactor bed. The reactor inlet temperature is 610 °C, the inlet CH_4 fraction is 0.90, and O_2 mole fraction is 0.10 ($CH_4/O_2 = 9$).

gas-phase reactions are initiated within the front quartz wool section. However, because the temperature is relatively low in this region (≈ 650 °C), the CH_4 conversion is very low.

As the gases enter the catalytic region, the rapid decrease in the oxygen concentration aligns with the consumption of methane (Figure 3). The oxygen is consumed fully by 9 mm. The O_2 and CH_4 concentration profiles indicate that methane conversion is limited by oxygen availability. The primary gas-phase products are C_2, CO_x, and H_2O, which reach their maximum values as the O_2 is consumed fully. The rapid exothermic oxidation contributes to a rapid temperature increase, and the temperature exceeds 750 °C by 9 mm from the reactor inlet (4 mm of quartz and 5 mm of active catalyst). The elevated temperature increases the formation rates of $CH_3^{\bullet}$ and C_2. However, the elevated temperature also contributes to competitive total oxidation, which leads to CO and CO_2 on the downstream sections of the catalyst bed.

The C_2H_4 profile develops more slowly than that of O_2 and CH_4 (Figure 3), but is comparable to the C_2H_6 and CO_2 profiles. This behavior suggests that C_2H_4 formation proceeds by C_2H_6 dehydrogenation. Additionally, the CO, CO_2, H_2O, and H_2 profiles show that their formation begins earlier than C_{2+} formation. This indicates that direct CH_4 oxidation is dominant. By the 12 mm position within the bed, all the species have effectively reached their asymptotic values. However, as a result of heat loss to the external environment (i.e., the relatively cool furnace walls), the temperature profile decreases.

Spatial profiles of the CH_4 conversion and the C_{2+} and CO_x yields are shown in Figure 4a. Within the front-side quartz wool, at which only the gas-phase reactions are active, the CH_4 conversion is less than 0.5 %. However, within the first 5 mm of the catalyst bed, both the CH_4 conversion and the C_{2+} and CO_x yields reach their maximum values.

Spatial profiles of the C_2H_6 and C_2H_4 selectivities are shown in Figure 4b. The primary gas-phase product formed within the first 2 mm of the front-side quartz wool section is C_2H_6. As the reactor temperature and CH_4 conversion increase within the bed, C_2H_6 becomes dehydrogenated to produce C_2H_4. At the 3 mm location within the front-side quartz wool, the C_2H_6 selectivity decreases sharply. However, the C_2H_4 selectivity increases only slightly because of competitive CO_x production.

5.1.1. CO_x formation pathways

CO_x and C_{2+} formation occurs essentially simultaneously (Figure 4a). Both surface and gas-phase reaction mechanisms include direct and indirect CO_x formation pathways. The direct gas-phase oxidation path is dominated by the reaction of $CH_3^{\bullet}$ with O_2 to form $CH_3O^{\bullet}$ and $CH_2O^{\bullet}$ (Reactions 6 and 7 in Table 2). The indirect CO_x formation occurs in the gas-phase by the reaction of C_2H_4 with O_2 (Reaction 23), $H^{\bullet}$ (Reaction 24), $OH^{\bullet}$ (Reaction 25), and $CH_3^{\bullet}$ (Reaction 26) to form $C_2H_3^{\bullet}$. On the catalyst surface, the direct oxidation proceeds by the reaction of $CH_3^{\bullet}$ with O(s) (Reaction 13 in Table 3) to form $CH_3O(s)$. The indirect oxidation of C_2H_4 occurs by the reaction of C_2H_4 with O(s) to form $C_2H_3^{\bullet}$ (Reaction 5 in Table 3) or to form $C_2H_4O(s)$ (Reaction 27 in Table 3).

The contribution of gas-phase and surface reactions to form CO_x depends on the local oxygen concentration and temperature. Reaction pathway diagrams for CO and CO_2 formation at three locations within the catalytic bed are shown in Figure 5. The reaction pathway diagram at the beginning of the catalyst bed at which the local temperature is 660 °C is shown in
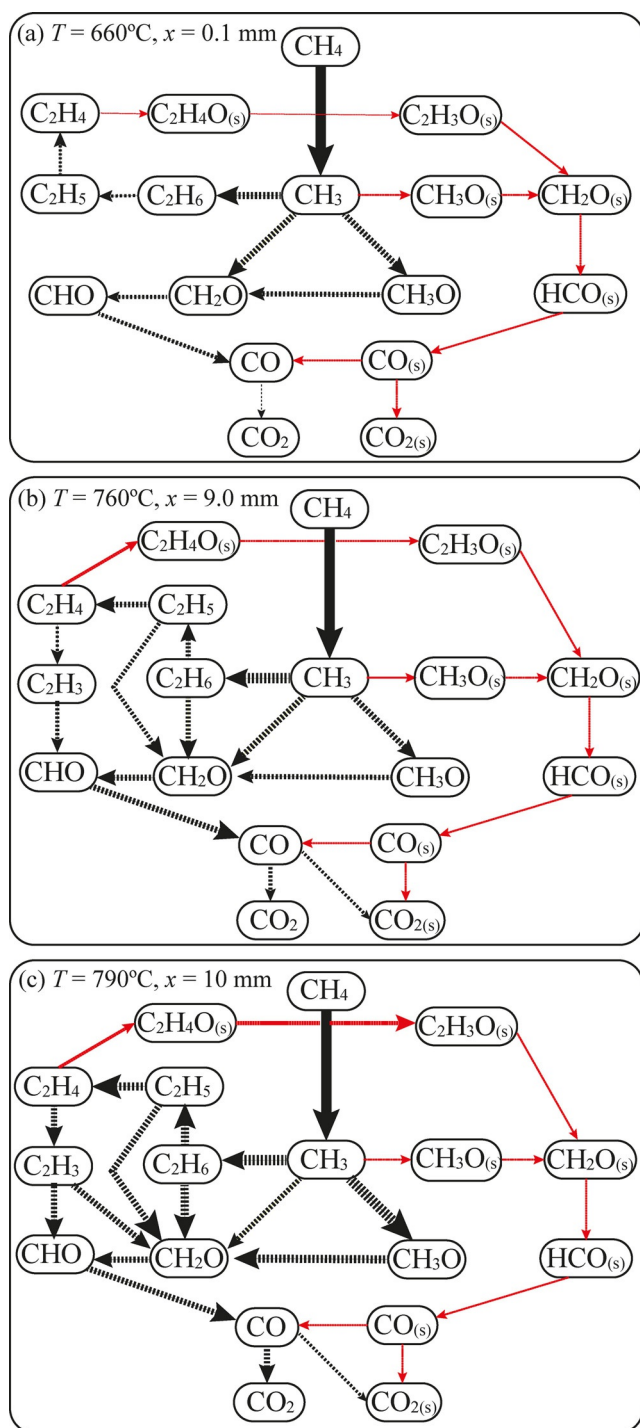
Figure 5. Contribution of reaction pathways to form CO and CO_2 at three axial positions within the reactor. The thickness of the arrows represents the magnitude of the reaction rates. Gas-phase reactions are shown as dashed lines, and the surface reactions are shown as red solid arrows. The black arrows indicate the combination of gas-phase and surface reactions.

Figure 5a. The direct oxidation pathway in the gas-phase is dominant at this relatively low temperature. After the formation of CH_3, the gas-phase oxidation of CH_3 forms CH_3O and CH_2O by Reactions 6 and 7 (Table 2), and then CHO by Reactions 10–13, and finally CO and CO_2. The direct and indirect surface reaction contributions to CO_x formation are relatively

weak (Figure 5a). The reaction pathways at the local temperature of 760 °C are shown in Figure 5b. A this point, the contribution from indirect gas-phase oxidation becomes significant. Between 0.1 and 9 mm, temperature affects the reaction pathways similarly. In this region, the contribution of gas-phase reactions to CO_x formation increases linearly as a function of temperature. The oxidation of C_2H_4 and C_2H_6 is the dominant pathway for CO and CO_2 formation. At 760 °C, C_2H_4 oxidation by O(s) to form $C_2H_4O(s)$ is also significant. The reaction pathways at 790 °C are shown in Figure 5c. The direct gas-phase oxidation pathway for the consumption of C_2H_4 and C_2H_6 is dominant. A significant increase in $C_2H_3O(s)$ formation from the dehydrogenation of $C_2H_4O(s)$ with O(s) (Table 3, Reaction 27) contributes greatly to CO and CO_2 formation.

5.1.2. H_2O formation pathways

Rate analysis similar to the CO_x study was also performed for H_2O formation. At low temperature (660 °C), the direct oxidation of CH_4 with $OH^·$ (Reaction 4 in Table 2) occurs primarily in the gas phase. Moreover, $CH_2O^·$ oxidation with $OH^·$ (Reaction 11 in Table 2) can produce H_2O as well, which is analogous to the pathway for the formation of CO and CO_2. The other two primary gas-phase reactions that contribute to H_2O formation are the oxidation of C_2H_4 and C_2H_6 with $OH^·$ (Reactions 18 and 25). As Reactions 18 and 25 are fast and nearly equilibrated, an increase of the H_2O concentration tends to shift the reactions in the reverse direction, which decreases the C_2 oxidation to form CO_x and, thus, increases the C_{2+} yield. This behavior is consistent with the observations by Takanabe and Iglesia on the Mn/Na_2WO_4/SiO_2 catalyst[38] and by Liang et al. on the same catalyst without Mn.[65]

Gas-phase H_2O also reacts on the catalyst surface to form OH(s), which affects the heterogeneous methane activation directly. The reverse reaction rate for methane activation depends on the OH(s) concentration (CH_3+OH(s)→CH_4+O(s)). Similarly, the oxidation of C_2H_6 and C_2H_4 by surface reactions also depends on the OH(s) concentration. Thus, high OH(s) concentrations can decrease the indirect oxidation of C_2. Takanabe and Iglesia[38] used a Mn/Na_2WO_4/SiO_2 catalyst to show experimentally that the introduction of low levels of H_2O (≈0.4%) in the feed CH_4/O_2 mixture could improve the methane conversion and C_2 selectivity.[38]

5.2. Effect of feed composition: CH_4/O_2 = 7

The modeled and measured gas-phase profiles for a feed mixture of CH_4/O_2 = 7 are shown in Figure 6. Similar to the case of CH_4/O_2 = 9, the methane conversion is limited by the oxygen availability. Rapid O_2 consumption contributes to rapid temperature increases, and the peak temperature was achieved within the first 5 mm of the catalyst bed. At the point of maximum temperature, all the species profiles had reached their asymptotic levels. Although the indirect oxidation path is not observed directly, a rate analysis indicates that the contribution of C_2H_4 and C_2H_6 become significant at high temperatures. The modeled profiles agree well with the measured profiles. The
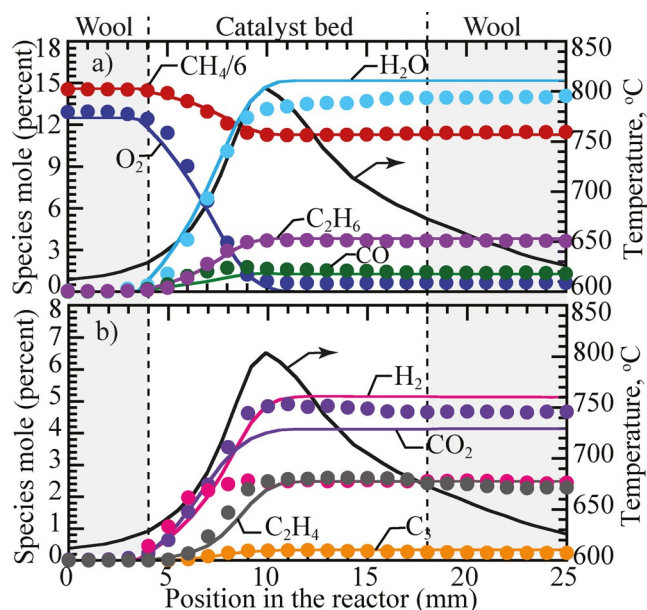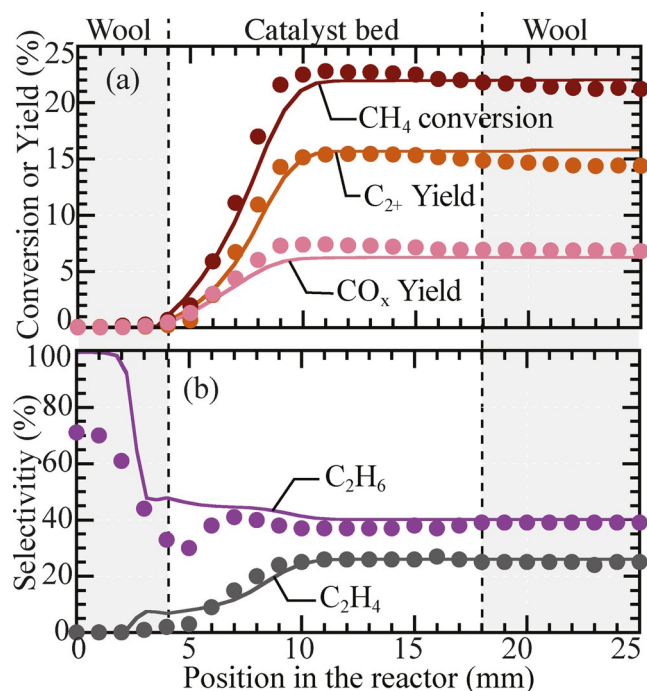
Figure 6. Comparison of measured (symbols) and predicted (lines) concentration and temperature profiles along the reactor bed. The reactor inlet temperature is 570 °C, the inlet CH_4 fraction is 0.875, and O_2 mole fraction is 0.125 ($CH_4/O_2 = 7$).

Figure 7. Comparison of measured (symbols) and predicted (lines) reactor performance. a) Profiles of methane conversion and yield. b) C_2 selectivity profiles. The reactor inlet temperature is 570 °C, the inlet CH_4 fraction is 0.875, and O_2 mole fraction is 0.125 ($CH_4/O_2 = 7$).

model predicts the early formation of H_2 just at the entrance to the active catalyst bed, which is consistent with the experimental observation. However, the model predicts significantly higher H_2 mole fractions than are measured. This issue is discussed further in Section 5.4.

Compared to the results presented in Figure 4 a, the methane conversion and C_{2+} yields increase slightly with the increase of the amount of oxygen in the gas mixture (Figure 7 a). A slight increase in the CO_x yield is also noticeable. Despite the noticeable decrease in the C_2H_6 mole fraction (i.e., 43 % at $CH_4/O_2 = 9$ compared to 37 % at $CH_4/O_2 = 7$), the C_2H_4 selectivity remains almost the same (i.e., ≈ 26 %; Figure 7 b).

5.3. Effect of feed composition: $CH_4/O_2 = 11$

The measured and predicted mole fraction profiles with $CH_4/O_2 = 11$ are shown in Figure 8. A decrease of the inlet oxygen concentration leads to the requirement of a higher temperature (i.e., 700 °C) to initiate reactions. Profiles of the desired C_{2+} products and the total-oxidation products CO_x generally follow trends that are similar to those with higher oxygen feeds. Compared to the cases of $CH_4/O_2 = 9$ and 7, the profiles for $CH_4/O_2 = 11$ develop more slowly. This could be caused by lower heat release rates and lower temperatures. As the O_2 concentration decreases, total oxidation and hence the heat release is much lower than that for the more O_2-rich conditions. The results shown in Figures 7 a and b support this possibility. At $CH_4/O_2 = 11$ the methane conversion is lower than that for the $CH_4/O_2 = 9$ and 7 inlet conditions, but the C_{2+} selectivity is higher (77 % at $CH_4/O_2 = 11$ and 68 % at $CH_4/O_2 = 7$). However, because the methane conversion is much lower at $CH_4/O_2 = 11$ than it is at $CH_4/O_2 = 9$ and 7, the overall C_{2+} yield is lower.
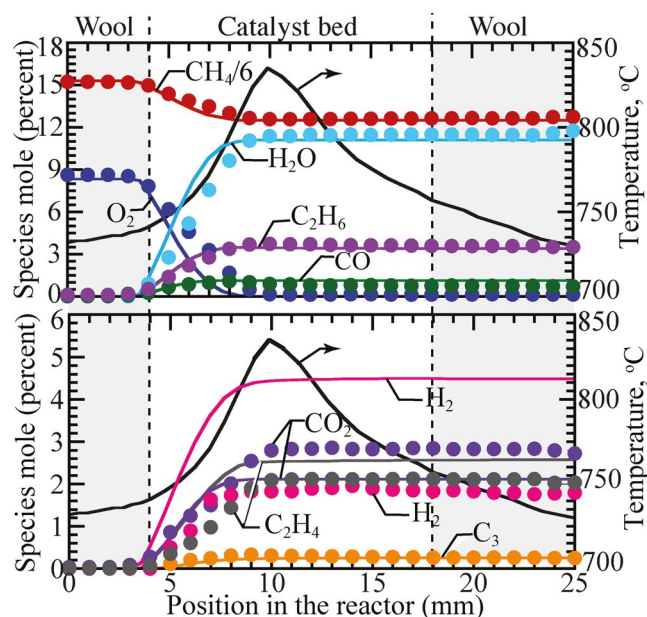
Figure 8. Comparison of measured (symbols) and predicted (lines) concentration and temperature profiles along the reactor bed. The reactor inlet temperature is 700 °C, the inlet CH_4 fraction is 0.9167, and O_2 mole fraction is 0.0833 ($CH_4/O_2 = 11$).

A significantly nonlinear trend between the CH_4 conversion and C_2 yield is shown in Figures 4, 7 and 9. The methane conversion increases with the increasing O_2 ratio in the feed as O_2 is the limiting reactant in OCM chemistry. A relatively high O_2 content in the feed stream increases the rate of total oxidation,
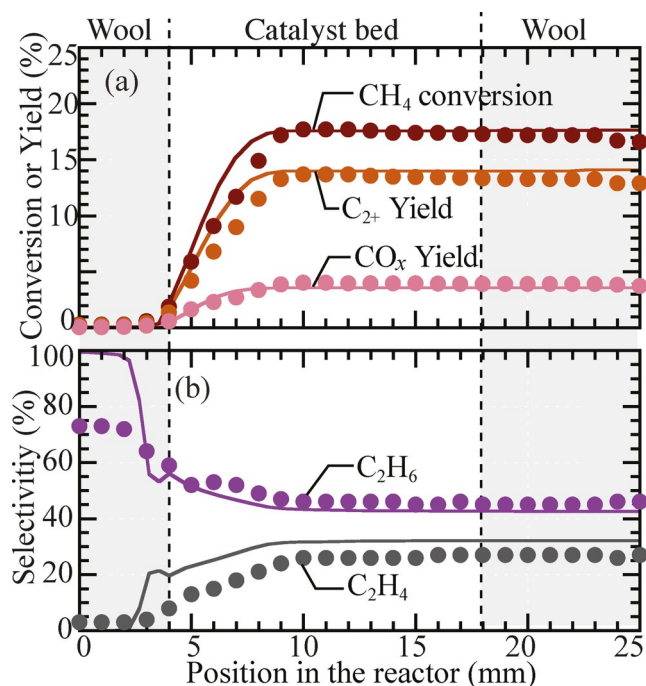
Figure 9. Comparison of measured (symbols) and predicted (lines) reactor performance. a) Profiles of methane conversion and yield. b) C_2 selectivity profiles. The reactor inlet temperature is 700 °C, the inlet CH_4 fraction is 0.9167, and O_2 mole fraction is 0.0833 ($CH_4/O_2 = 11$).

which is exothermic and results in a greater heat release. As the temperature increases, methane conversion and hence the $CH_3^{\bullet}$ formation rate increases. Consequently, the C_{2+} formation rate increases. However, at high temperatures, indirect CO_x formation by gas-phase and surface reactions becomes increasingly significant with the deleterious oxidative consumption of C_2H_4 and C_2H_6.

Coke formation and catalyst durability introduce another practical aspect for adjusting the CH_4/O_2 ratios. As is evident from the concentration profiles, O_2 is consumed rapidly and only a few mm (≈ 5 mm) of the catalyst bed operates in an oxidative environment. As the profiles develop fully and the temperatures are high, the hydrocarbons (i.e., CH_4 and C_{2+}) react in an oxygen-deficient environment. At high temperatures (> 700 °C) and under nonoxidative conditions, the dehydrogenation of CH_4 and C_2 can form coke or other condensable hydrocarbon deposits easily. Although no significant coke was detected during the catalytic measurements within the 24 h tests, gradual catalyst deactivation might occur with long-term operation.

The local heat release rates and temperature increases are coupled directly with O_2 consumption. Consequently, as an alternative to premixing the CH_4/O_2 feed stream, it should be possible to control the heat release and C_2 oxidation by introducing the O_2 axially along the length of the catalyst bed. Zohour et al.[66] showed that the C_{2+} yield increases by approximately 30% with the injection of O_2 at two positions within the catalyst bed. In these experiments, the total O_2 input was the same as in the initially premixed case. It should be possible to optimize the number injection ports and the O_2
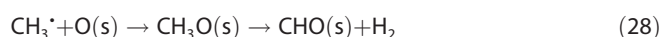
introduction rates to increase C_2 yield.[4,67–69] As an alternative to multiple O_2 injection ports, porous or ion transport O_2 membranes could also be used to supply O_2 along the axial length of the reactor. Such strategies seek to avoid local hot spots and any deleterious secondary oxidation reactions.[70–75]

5.4. H₂ formation

As noted in the foregoing discussion, there are significant discrepancies between the magnitudes of the modeled and measured H_2 profiles. The modeled results are systematically higher than the reported measurements.[49] Inasmuch as all the other species profiles agree well, the H_2 discrepancy is surprising. Thus, some further analysis based on hydrogen atomic balances is developed to seek resolution and possibly to reinterpret the measurements.
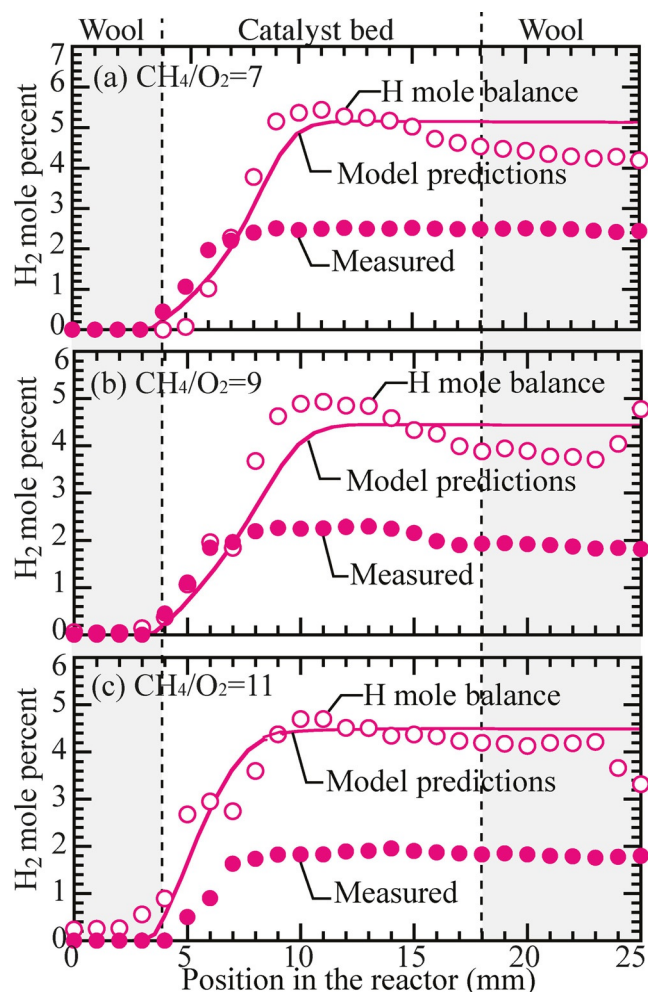
A comparison of the revised and measured H_2 profiles with the model predictions for the three CH_4/O_2 ratios is shown in Figure 10. The filled symbols represent the reported measurements, and the empty symbols represent the "measurements" revised by the atomic hydrogen balances from all other measured gas-phase species. In other words, the revised H_2 measurements preserve the hydrogen atom balance. The model predictions are in good agreement with the revised H_2 profiles (Figure 10). Thus, there is reason to suspect some inaccuracy in the H_2 measurements reported initially. In all cases, the H_2 levels are low, with mole fractions in the range of 1–5%.

Zohour et al.[49] noted the "early" appearance of H_2 relative to the other gas-phase species near the beginning of the active catalyst section. They postulated that a sequence of surface reactions could be responsible for early H_2 formation as [Eqs. (25)–(31)]:

$$CH_3^{\bullet} + OH(s) \rightarrow CH_2O(s) + H_2 \tag{25}$$

$$CH_2O(s) \rightarrow La(s) + CO(s) + H_2 \tag{26}$$

$$CO(s) + O(s) \rightarrow La(s) + CO_2 \tag{27}$$

$$CH_3^{\bullet} + O(s) \rightarrow CH_3O(s) \rightarrow CHO(s) + H_2 \tag{28}$$

$$CHO(s) + O(s) \rightarrow La(s) + H(s) + CO_2 \tag{29}$$

$$CHO(s) \rightarrow H(s) + CO \tag{30}$$

$$H(s) + H(s) \rightarrow 2 La(s) + H_2 \tag{31}$$

In these reactions we assume that H(s) is formed on the surface, and all such reactions are included in Table 3. However, as an alternative to the formation of H(s) on the surface, we also include the possibility of the heterogeneous oxidation of $CH_2O(s)$ and $CHO(s)$ to form OH(s) (i.e., Table 3, Reactions 15, 17, and 19). Although these surface reaction pathways do not affect H_2 formation directly, they do act to promote gas-phase H_2O and H_2 production.

The model predicts the early H_2 formation successfully, which is generally in good agreement with the experiments (Figures 6–8). H_2 begins to form immediately at the beginning of the catalytic region, which suggests a direct reaction pathway. A rate analysis confirms that the H_2 forms directly by a

Figure 10. Comparison of model-predicted H_2 profiles with reported and revised measurements for three CH_4/O_2 ratios. The revised measurements are based on hydrogen atom balances and other species measurements.

gas-phase reaction. Reaction 2 in Table 2 ($CH_4 + H \rightleftarrows CH_3^{\bullet} + H_2$) is the primary pathway for H_2 production. $H^{\bullet}$ is formed primarily by $CHO^{\bullet} + M \rightleftarrows CO + H^{\bullet} + M$ (Table 2, Reaction 14). At temperatures above 750 °C, C_2H_6 and C_2H_4 dehydrogenation reactions form $H^{\bullet}$, which also contributes to H_2 formation by Reactions 16, 20, and 23 in Table 2.

6. Summary and Conclusion

We develop detailed and predictive reaction mechanisms that represent gas-phase and surface chemistry for the oxidative coupling of methane over nanofabric La_2O_3/CeO_2 catalysts. The gas-phase reaction mechanism includes 39 reversible reactions between 22 species. The surface mechanisms include 52 irreversible reactions between 11 surface species and 16 gas-phase species. The chemistry is developed and validated in concert with measured gas-phase species profiles in a packed-bed reactor. Electronic versions of the reaction mechanisms and related thermodynamic and transport files are provided as Supporting Information.

The reaction mechanisms represent a comprehensive picture of nonisothermal oxidative coupling of methane (OCM) chemistry with nanofabric La_2O_3/CeO_2 catalysts. The starting point for the gas-phase reaction mechanism was taken from Chen et al.[33] The surface-reaction pathway was taken from the study by Alexiadis et al.[31] in which the Sr/La_2O_3 catalyst was considered. Earlier studies suggested that OCM reaction pathways are similar even for different catalysts such as Li/MgO, Sr/La_2O_3, and $Mn/Na_2WO_4/SiO_2$. With such general similarity in mind, in this study we have extended earlier work to develop a new reaction mechanism for the nanofabric La_2O_3/CeO_2 catalyst. As a result of the expected similarity, the present detailed reaction mechanisms also serve as a foundation for extension to other OCM catalysts.

The mechanism development is based on unique spatially resolved concentration and temperature measurements in a packed-bed reactor.[49] Compared to typical packed-bed experiments from which only gas-phase species measurements in the exit flow are reported, the spatially resolved species profiles offer enormous value to understand reaction pathways. Gas-phase reactions are the dominant pathways for CO_x formation, whereas heterogeneous reactions on the catalyst contribute significantly to CH_4 activation. The catalyst also serves as an O_2 pool, and O_2 adsorption and desorption behavior controls the O_2 that is available in the gas phase and hence the formation of total oxidation products.

Results of the study show that CH_4 activation proceeds by the coupled interactions of the gas-phase and surface reactions. Initially, exothermic gas-phase oxidation provides the reaction heat and elevated temperature needed to activate surface reactions. Methane conversion is limited by oxygen availability in the feed stream, and the desired C_2 formation rate is controlled by the $CH_3^{\bullet}$ that is produced by gas-phase and surface reactions. Broadly speaking, the La_2O_3/CeO_2 catalyst controls the gas-phase chemistry by controlling the oxygen adsorption–desorption rates. Practical OCM technology depends on balancing the desired C_{2+} production and the undesired deep oxidation to CO, CO_2, and H_2O. As the deep oxidation is thermodynamically favored, technologically viable process design and control can be challenging. The predictive understanding that emerges from detailed reaction mechanisms is expected to play a valuable role in process design, control, and optimization of practical technology.

Conflict of interest

The authors declare no conflict of interest.

[1] G. E. Keller, M. M. Bhasin, *J. Catal.* **1982**, *73*, 9–19.
[2] E. F. Lutz, *J. Chem. Educ.* **1986**, *63*, 202–203.
[3] M. Lallemand, A. Finiels, F. Fajula, F. Hulea, *Appl. Catal. A* **2006**, *301*, 196–201.
[4] S. C. Reyes, E. Iglesia, C. P. Kelkar, *Chem. Eng. Sci.* **1993**, *48*, 2643–2661.
[5] J. H. Lunsford, *Catal. Today* **2000**, *63*, 165–174.
[6] H. R. Godini, S. Xiao, S. Jaso, G. Wozny, *Fuel Process. Technol.* **2013**, *106*, 684–694.
[7] S. Stünkel, D. Illmer, A. Drescher, R. Schomäcker, G. Wozny, *Appl. Therm. Eng.* **2012**, *43*, 141–147.
[8] R. P. Taylor, G. L. Schrader, *Ind. Eng. Chem. Res.* **1991**, *30*, 1016–1023.
[9] T. Levan, M. Che, J. M. Tatibouet, M. Kermarec, *J. Catal.* **1993**, *142*, 18–26.
[10] K. D. Campbell, H. Zhang, J. H. Lunsford, *J. Phys. Chem.* **1988**, *92*, 750–753.
[11] J. M. DeBoy, R. F. Hicks, *J. Catal.* **1988**, *113*, 517–527.
[12] M. T. Xu, J. H. Lunsford, *Catal. Lett.* **1991**, *11*, 295–300.
[13] V. R. Choudhary, S. A. R. Mulla, V. H. Rane, *J. Chem. Technol. Biotechnol.* **1998**, *72*, 125–130.
[14] P. Huang, Y. Zhao, J. Zhang, Y. Zhu, Y. Sun, *Nanoscale* **2013**, *5*, 10844–10848.
[15] Y. Lei, C. Chu, S. Li, Y. Sun, *J. Phys. Chem. C* **2014**, *118*, 7932–7945.
[16] Y. H. Hou, W. C. Han, W. S. Xia, H. L. Wan, *ACS Catal.* **2015**, *5*, 1663–1674.
[17] D. Noon, A. Subsai, S. Senkan, *ChemCatChem* **2013**, *5*, 146–149.
[18] J. Song, Y. Sun, R. Ba, S. Huang, Y. Zhao, J. Zhang, Y. Sun, Y. Zhu, *Nanoscale* **2015**, *7*, 2260–2264.
[19] Z. Stansch, L. Mleczko, M. Baerns, *Ind. Eng. Chem. Res.* **1997**, *36*, 2568–2579.
[20] Y. Feng, J. Niiranen, D. Gutman, *J. Phys. Chem.* **1991**, *95*, 6558–6563.
[21] G. S. Lane, E. E. Wolf, *J. Catal.* **1988**, *113*, 144–163.
[22] K. Otsuka, Y. Uragami, M. Hatano, *Catal. Today* **1992**, *13*, 291–300.
[23] B. Beck, V. Fleisher, S. Arndt, M. G. Hevia, A. Urakawa, P. Hugo, R. Schomacher, *Catal. Today* **2014**, *228*, 212–218.
[24] K. D. Campbell, J. H. Lunsford, *J. Phys. Chem.* **1988**, *92*, 5792–5796.
[25] D. J. Driscoll, W. Martir, J. X. Wang, J. H. Lunsford, *J. Am. Chem. Soc.* **1985**, *107*, 58–63.
[26] Y. D. Tong, M. P. Rosynek, J. H. Lunsford, *J. Phys. Chem.* **1989**, *93*, 2896–2898.
[27] L. Luo, X. Tang, W. Wang, Y. Wang, S. Sun, F. Qi, W. Huang, *Sci. Rep.* **2013**, *3*, 1625–1631.
[28] J. Sun, J. W. Thybaut, G. B. Marin, *Catal. Today* **2008**, *137*, 90–102.
[29] J. W. Thybaut, J. Sun, L. Olivier, A. C. V. Veen, C. Mirodatus, G. B. Marin, *Catal. Today* **2011**, *159*, 29–36.
[30] J. W. Thybaut, G. B. Marin, C. Mirodatos, Y. Schuurman, A. C. van Veen, V. A. Sadykov, H. Pennemann, L. Bellinghausen, L. Mleczko, *Chem. Ing. Tech.* **2014**, *86*, 1855–1870.
[31] V. I. Alexiadis, J. W. Thybaut, P. N. Kechagiopoulis, M. Chaar, A. C. Van Veen, M. Muhler, G. B. Marin, *Appl. Catal. B* **2014**, *150*, 496–505.
[32] V. I. Alexiadis, M. Chaar, A. van Veen, M. Muhler, J. W. Thybaut, G. B. Marin, *Appl. Catal. B* **2016**, *199*, 252–259.
[33] Q. Chen, P. M. Couwenberg, G. B. Marin, *AIChE J.* **1994**, *40*, 521–535.
[34] J. Warnatz, *Rate coefficients in the C/H/O system in combustion chemistry*, Springer, Berlin, **1984**.
[35] G. P. Smith, D. M. Golden, M. Frenchlach, N. W. Moriarty, B. Eiteneer, M. Goldenberg, C. T. Bowman, R. K. Hanson, S. Song, W. C. Gardiner Jr., V. V. Lissianski, Z. Qin, GRI Mechanism Version 3.0, **1999**.
[36] S. Dooley, M. P. Burke, M. Chaos, Y. Stein, F. L. Dryer, O. Finch, J. M. Simmie, H. J. Curran, *Int. J. Chem. Kinet.* **2010**, *42*, 527–549.
[37] Q. Chen, J. H. B. J. Hoebink, G. B. Marin, *Ind. Eng. Chem. Res.* **1991**, *30*, 2088–2097.
[38] K. Takanabe, E. Iglesia, *Angew. Chem. Int. Ed.* **2008**, *47*, 7689–7693; *Angew. Chem.* **2008**, *120*, 7803–7807.
[39] J. H. Lunsford, *Angew. Chem. Int. Ed. Engl.* **1995**, *34*, 970–980; *Angew. Chem.* **1995**, *107*, 1059–1070.
[40] J. A. Miller, C. T. Bowman, *Prog. Energy Combust. Sci.* **1989**, *15*, 287338.
[41] H. Zanthoff, M. Baerns, *Ind. Eng. Chem. Res.* **1990**, *29*, 2–10.
[42] C. A. Mims, R. Mauti, A. M. Dean, K. D. Rose, *J. Phys. Chem.* **1994**, *98*, 13357–13372.
[43] H. Wang, X. You, A. V. Joshi, S. G. Davis, A. Laskin, F. Egolfopoulos, C. K. Law, *High temperature combustion reaction model of H2/CO/C1-C4 compounds*, University of Southern California, **2007**, http://ignis.usc.edu/USC~Mech~II.htm.
[44] J. G. Lopez, C. L. Rasmussen, M. U. Alzueta, Y. Gao, P. Marshall, P. Glarborg, *Proc. Combust. Inst.* **2009**, *32*, 367–375.
[45] A. A. Konnov, *Combust. Flame* **2009**, *156*, 2093–2105.
[46] R. Dittmeyer, PhD thesis, Universität Erlangen-Nürnberg, **1994**.
[47] S. Mavlyankariev, PhD thesis, Technische Universität Berlin, **2013**.
[48] R. Horn, K. A. Williams, N. J. Degenstein, L. D. Schmidt, *J. Catal.* **2006**, *242*, 92–102.
[49] B. Zohour, D. Noon, S. Senkan, *ChemCatChem* **2013**, *5*, 2809–2812.
[50] Y. Simon, F. Baronnet, P.-M. Marquaire, *Ind. Eng. Chem. Res.* **2007**, *46*, 1914–1922.
[51] M. Yu. Sinev, *Catal. Today* **1992**, *13*, 561–564.
[52] M. Yu. Sinev, B. Yu. Bychkov, V. N. Korchak, O. V. Krylov, *Catal. Today* **1990**, *6*, 543–549.
[53] M. Yu. Sinev, *Catal. Today* **1995**, *24*, 389–393.
[54] M. Yu. Sinev, *Russ. J. Phys. Chem. B* **2007**, *1*, 412–433.
[55] M. Yu. Sinev, Z. T. Fattakhova, V. I. Lomonosov, Yu. A. Gordienko, *J. Nat. Gas Chem.* **2009**, *18*, 273–287.
[56] P. N. Kechagiopoulos, J. W. Thybaut, G. B. Marin, *Ind. Eng. Chem. Res.* **2014**, *53*, 1825–184021.
[57] Y. S. Su, J. Y. Ying, W. H. Green Jr., *J. Catal.* **2003**, *218*, 321–333.
[58] R. J. Kee, M. E. Coltrin, P. Glarborg, *Chemically Reacting Flow*, Wiley, Hoboken, NJ, **2003**.
[59] M. E. Coltrin, R. J. Kee, F. M. Rupley, *Int. J. Chem. Kinet.* **1991**, *23*, 1111–1128.
[60] L. Maier, N. Schaedel, K. H. Delgado, S. Tisher, O. Deutschmann, *Top. Catal.* **2011**, *54*, 845–858.
[61] M. Maestri, D. G. Vlachos, A. Beretta, G. Groppi, E. Tronconi, *J. Catal.* **2008**, *259*, 211–222.
[62] D. Noon, B. Zohour, S. Senkan, *J. Nat. Gas Sci. Eng.* **2014**, *18*, 406–411.
[63] H. Zhu, R. J. Kee, J. R. Engel, D. T. Wickham, *Proc. Combust. Inst.* **2007**, *31*, 1965–1972.
[64] P. Deuflhard, E. Hairer, J. Zugck, *Numer. Math.* **1987**, *51*, 501–516.
[65] Y. Liang, Z. Li, M. Nourdine, S. Shahid, K. Takanabe, *ChemCatChem* **2014**, *6*, 1245–1251.
[66] B. Zohour, D. Noon, S. Senkan, *ChemCatChem* **2014**, *6*, 2815–2820.
[67] J. M. Santamaria, E. E. Miro, E. E. Wolf, *Ind. Eng. Chem. Res.* **1991**, *30*, 1157–1165.
[68] J. Santamaría, M. Menéndez, J. A. Peña, J. I. Barahona, *Catal. Today* **1992**, *13*, 353–360.
[69] I. P. Androulakis, S. C. Reyes, *AIChE J.* **1999**, *45*, 860–868.
[70] Y. Zeng, Y. S. Lin, S. L. Swartz, *J. Membr. Sci.* **1998**, *150*, 87–98.
[71] Z. Shao, H. Dong, G. Xiong, Y. Cong, W. Yang, *J. Membr. Sci.* **2001**, *183*, 181–192.
[72] O. Czuprat, T. Schiestel, H. Voss, J. Caro, *Ind. Eng. Chem. Res.* **2010**, *49*, 10230–10236.
[73] H. R. Godini, S. Jaso, S. Xiao, H. Arellano-Garcia, M. Omidkhah, G. Wozny, *Ind. Eng. Chem. Res.* **2012**, *51*, 7747–7761.
[74] H. R. Godini, H. Trivedi, A. Gili de Villasante, O. Gorke, S. Jaso, U. Simon, A. Berthold, W. Witt, G. Wozny, *Chem. Eng. Res. Des.* **2013**, *91*, 2671–2681.
[75] N. H. Othman, Z. Wu, K. Li, *J. Membr. Sci.* **2015**, *488*, 182–193.